An Ultrasonic Energy Harvesting IC Providing Adjustable Bias Voltage for Pre-Charged CMUT

Linran Zhao, *Graduate Student Member*, *IEEE*, Muhammetgeldi Annayev, *Graduate Student Member*, *IEEE*, Ömer Oralkan, *Senior Member*, *IEEE*, Yaoyao Jia, *Member*, *IEEE*

***Abstract*—Ultrasonic wireless power transmission (WPT) using pre-charged capacitive micromachined ultrasonic transducers (CMUT) is drawing great attention due to the easy integration of CMUT with CMOS techniques. Here, we present an integrated circuit (IC) that interfaces with a pre-charged CMUT device for ultrasonic energy harvesting. We implemented an adaptive high voltage charge pump (HVCP) in the proposed IC, which features low power, overvoltage stress (OVS) robustness, and a wide output range. The ultrasonic energy harvesting IC is fabricated in the 180 nm HV BCD process and occupies a 2 × 2.5 mm² silicon area. The adaptive HVCP offers a 2× – 12× voltage conversion ratio (VCR), thereby providing a wide bias voltage range of 4V – 44V for the pre-charged CMUT. Moreover, a VCR tunning finite state machine (FSM) implemented in the proposed IC can dynamically adjust the VCR to stabilize the HVCP output (i.e., the pre-charged CMUT bias voltage) to a target voltage in a closed-loop manner. Such a closed-loop control mechanism improves the tolerance of the proposed IC to the received power variation caused by misalignments, amount of transmitted power change, and/or load variation. Besides, the proposed ultrasonic energy harvesting IC has an average power consumption of 35 µW – 554 µW corresponding to the HVCP output from 4 V – 44 V. The CMUT device with a local surface acoustic intensity of 3.78 mW/mm², which is well below the FDA limit for power flux (7.2 mW/mm²), can deliver sufficient power to the IC.**

***Keywords*—ultrasonic energy harvesting, wireless power transmission, high voltage charge pump, pre-charged CMUT**

I. Introduction

IMPLANTABLE medical devices (IMD) that interface with the nervous system for recording and stimulating neural activities help deepen our understanding of the brain, revolutionize the way that the human interacts with computers and robotics, and enable neuromodulation-based therapies for neurological diseases and conditions, e.g., Alzheimer's disease, Parkinson's disease, and Epilepsy, which currently cannot be treated adequately with medication alone [1-3]. Wireless power transmission (WPT) is a key feature that can eliminate the tethering effects and the requirement of bulky batteries, bringing the IMDs closer to clinical use [1-3]. So far electromagnetic (EM) and ultrasonic WPT approaches have been commonly used, each of which has its advantages for a particular application [4, 5].

This work is supported in part by the National Science Foundation award ECCS-2151788 and in part by NC State University and the University of Texas at Austin.

L. Zhao and Y. Jia are with the Department of Electrical and Computer Engineering, The University of Texas at Austin, Austin, TX 78712, USA (e-mail: lrzhao@utexas.edu and yjia@austin.utexas.edu).

M. Annayev and Ö. Oralkan are with the Department of Electrical and Computer Engineering, North Carolina State University, Raleigh, NC 27695, USA (mannaye@ncsu.edu and ooralka@ncsu.edu).

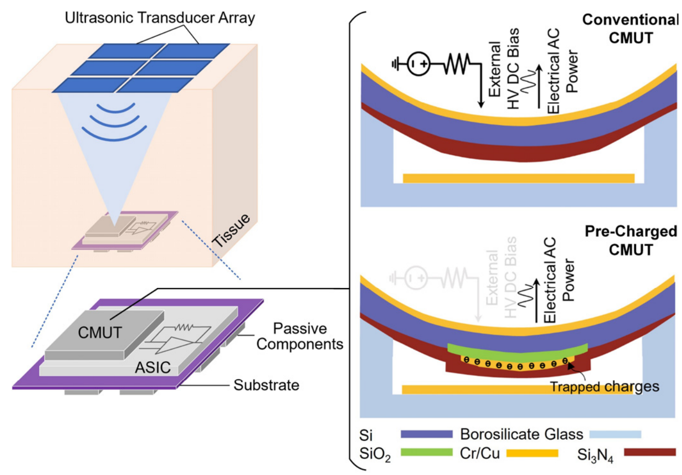

Fig. 1. Conceptual view of the ultrasonically powered IMD that incorporates a pre-charged CMUT to receive ultrasonic power at deep tissue.

Near-field inductive link and far-field RF link are two popular implementations of the EM WPT approach. Several inductive link designs implemented in wireless power cages enable high efficient WPT to an IMD carried by a small animal subject (e.g., a rodent) while the subject is freely moving inside the cage [6-8]. It is well understood that device miniaturization is significant in reducing device invasiveness to the tissue [1-3]. However, WPT to mm/sub-mm sized IMDs is challenging. The weak coupling between transmitter (Tx) and receiver (Rx) coils and stringent size constraints affects power transfer efficiency (PTE) and the amount of power delivered to the load (PDL) [9, 10]. To overcome these challenges, various inductive link configurations and optimization methods have been proposed [11-17]. Unlike large coils, tiny coils tend to have their optimal Q-factor at hundreds of MHz or even in GHz bands. However, the specific absorption rate (SAR) of the EM field in the body increases along with the carrier frequency [18]. This will limit the WPT depth in tissue and impose stringent safety constraints. Far-field RF links usually offer long-distance WPT through the air and have been used significantly in WPT to IMDs [19, 20]. However, most of the proposed designs are in the GHz band, which imposes more challenges on SAR limits.

This article has been accepted for publication in IEEE Transactions on Biomedical Circuits and Systems. This is the author's version which has not been fully edited and content may change prior to final publication. Citation information: DOI 10.1109/TBCAS.2022.3178581

Compared to EM WPT, the ultrasonic WPT approach has distinct advantages of shorter wavelength, lower attenuation in body tissue, and little EM interference [4, 5]. Thus, ultrasonic WPT has been widely used to power miniature IMDs in deep tissue without surpassing the FDA ultrasound intensity limit [21-23]. It is also feasible to apply beamforming of ultrasonic energy to mm-sized focal spots at large depths in the body [21, 22]. A great number of existing ultrasonic WPT designs use piezoelectric transducers [24-28]. In [24], the ultrasonically powered implant that incorporates a piezo and an integrated circuit (IC) can receive input power of several milliwatts with dimensions of 2×3×6.5 mm^3 at the tissue depth of 10.5 cm from a commercial Tx transducer operating at 1.3 MHz – 1.5 MHz. In the ultrasonically powered neural stimulation system presented in [25], a 1.7 mm^3 stimulator receives power at 18 mm in vivo depth through an ultrasonic link at 1.85 MHz. The ultrasonic link in [26] operates at 2 MHz, delivering ~140 μW amount of power to a 4.5mm^3 ultrasonic luminescence oxygen sensor implanted at 5 cm tissue depth. There are also ultrasonic WPT systems with phased array beamforming techniques that enable wireless powering of multiple implants [27, 28].

The advent of microelectromechanical system (MEMS) technology has brought about the development of capacitive micromachined ultrasonic transducer (CMUT). CMUT can be an alternative technology to the piezoelectric transduces with its distinct advantage of easy integration with electronic circuits [29-31]. Such feasibility is significant in IMD miniaturization. CMUT also features ease of fabrication and the possibility of achieving broader bandwidth [29-31]. In Fig. 1, the conceptual view of CMUT-based ultrasonic WPT shows that the CMUT-on-CMOS integration reduces the number of electrical connections leading to a smaller device form factor [32, 33]. This approach also minimizes parasitic capacitances, which would enhance the PTE of the ultrasonic link [32, 33]. However, standard CMUT requires an extra bias voltage in the order of several tens of volts to hundred volts, which sets a barrier for IMD power reduction [29-31]. To eliminate or moderate the requirement of the high DC bias, pre-charged CMUT is developed and used as the power Rx component for ultrasonic energy harvesting [34-36].

Fig. 1 shows a CMUT with a metal floating gate [36]. A chromium/gold layer is introduced inside the CMUT structure as a floating electrode to trap charges. The trapped charges replace the DC bias to produce a static plate deflection in the CMUT device, thus enabling CMUT to receive the amount of power that is just enough for ultrasonic energy harvesting circuits to start up without an external bias voltage. Once the circuits start up successfully, they, in turn, can provide a bias voltage, a few volts to tens of volts, such that the pre-charge CMUT can operate at its optimal condition in terms of maximum output power. The bias voltage that the circuits can provide varies as the amount of received power changes. To stabilize the bias voltage in different wireless power conditions, it would be significant that the ultrasonic energy harvesting circuits can provide a bias voltage dynamically adjustable in a closed-loop manner for the pre-charged CMUT.

Hence, we propose a novel ultrasonic energy harvesting IC, in which a low power, overstress robust, adaptive high voltage charge pump (HVCP) provides an adjustable bias voltage of 4 V – 44 V for the pre-charged CMUT. Such a wide bias voltage range enables the IC to meet the needs of the bias for a variety of pre-charge conditions. The HVCP is also applicable for electrical stimulation as it can offer sufficient compliance voltage for the stimulator. To the best of our knowledge, this is the first IC that interfaces with pre-charged CMUT for ultrasonic energy harvesting. An overview of the proposed ultrasonic energy harvesting IC is given in Section II. Section III presents the acoustic measurement setup. Section IV shows the IC characterization, followed by a discussion and a conclusion.

II. Ultrasonic Energy Harvesting IC Overview

The block diagram of the proposed ultrasonic energy harvesting IC is shown in Fig. 2. A voltage doubler converts the AC input voltage, V_{AC}, to a DC voltage, V_{DBR}, which is further regulated by a low-dropout regulator (LDO), resulting in a supply voltage of V_{DD} = 1.8V. A bandgap reference (BGR) and bias generator provide bias voltages/currents for the remaining circuits. As V_{DD} increases to a certain value, a power-on-reset (POR) flag raises to trigger digital control circuits. The HVCP employs a switched-capacitor-based structure in each stage, in

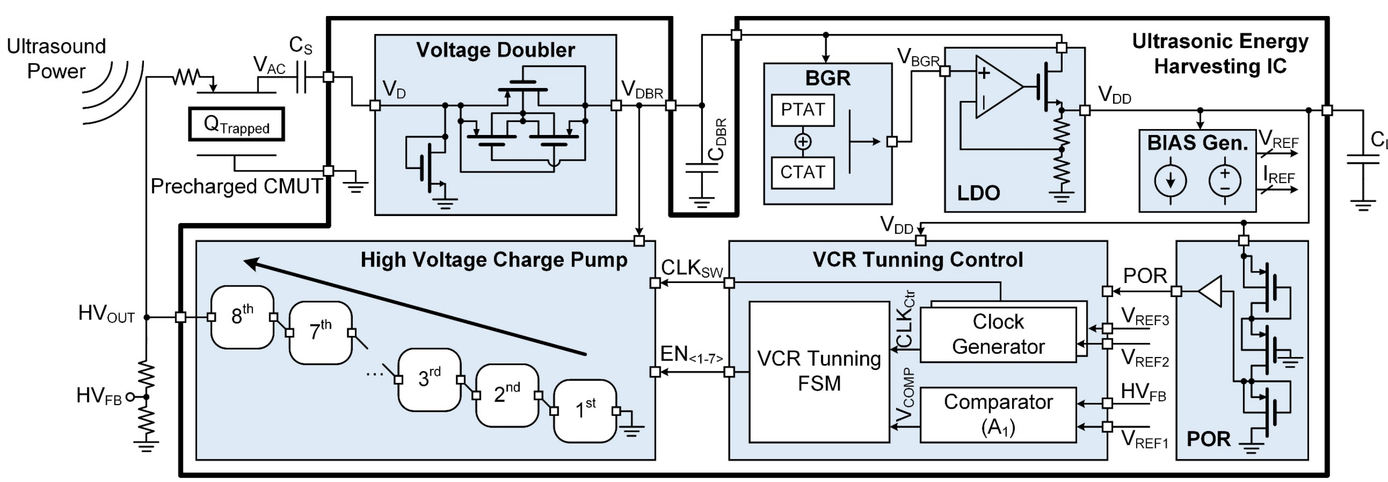

Fig. 2. Block diagram of the ultrasonic energy harvesting IC.

which a clock, CLK_{SW}, controls the capacitor switching, upconverting the HVCP input (i.e., V_{DBR}) to HV_{OUT} (i.e., the bias voltage for the CMUT). The voltage conversion ratio (VCR) tunning control circuits adjust the VCR of the HVCP to stabilize HV_{OUT} to a target voltage in a closed-loop manner. More specifically, the VCR tunning finite-state-machine (FSM), controlled by the clock, CLK_{Ctr}, generates controls bits, $EN_{<1-7>}$, based on the comparison result of the divided HV_{OUT}, HV_{FB}, and a reference voltage, V_{REF1}, to enable/disable the 8 stages in the HVCP.

Fig. 3a shows the HVCP schematic, which consists of 8 cascaded stages, i.e., the first four +1 cells and the last four +2 cells. As shown in Fig. 3b, the design of the +1 cell refers to the cross-coupled charge pump structure, in which the clocks, ϕ_1 and ϕ_2, generated from non-overlapping clocks, CLK_P and CLK_N, oscillate between V_{DBR} and GND. The +2 cell is configured as two +1 cells connected in series. Using non-overlapping clocks can reduce switching loss and flow-back leakage current, thereby saving the power consumption of HVCP. In Fig. 3c, the non-overlapping clocks, CLK_P and CLK_N, are generated from CLK_{SW} and stepped up from V_{DD} to V_{DBR}. The delay elements, i.e., inverters, influence the delays between CLK_P and CLK_N. We designed the size and the number of the inverters to ensure sufficient non-overlapping between CLK_P and CLK_N.

The proposed HVCP features overvoltage stress (OVS) robustness. In the cross-coupled charge pump structure, the maximum gate-to-source voltage is V_{DBR}, which is below the breakdown voltage. Such an HVCP cell design can mitigate the gate-to-source OVS issue. To tolerate the high drain-to-source voltage, 70V MOSFETs are used in HVCP cells and their corresponding switches, S_1-S_7. Each cell, except the 8th cell, has its HV switch connecting between the cell output and GND. If the switch is connected between the output of the nth cell and the input of the (n+1)th cell, boost-strap drivers are required to drive the gate of the floating switch MOSFET [37]. The current switch configuration simplifies the switch driver, thus reducing the HVCP power consumption.

$EN_{<1-7>}$ selectively control S_1-S_7 to set VCR as 2×, 4×, 6×, 8×, 9×, 10×, 11×, or 12×. Since the supply voltage of the charge pump cells and clocks in the HVCP is V_{DBR}, we can calculate HV_{OUT} using $HV_{OUT} = V_{DBR} \times \text{VCR} -$ voltage loss. In Fig. 3d, we present three examples of VCR settings via $EN_{<1-7>}$ controls. We enable a cell by turning off its HV switch at the output, otherwise, we need to turn on the switch to disable the cell. As we can see, the 8th cell is always enabled. To set the VCR to a certain value, we need to enable the last few cells by turning

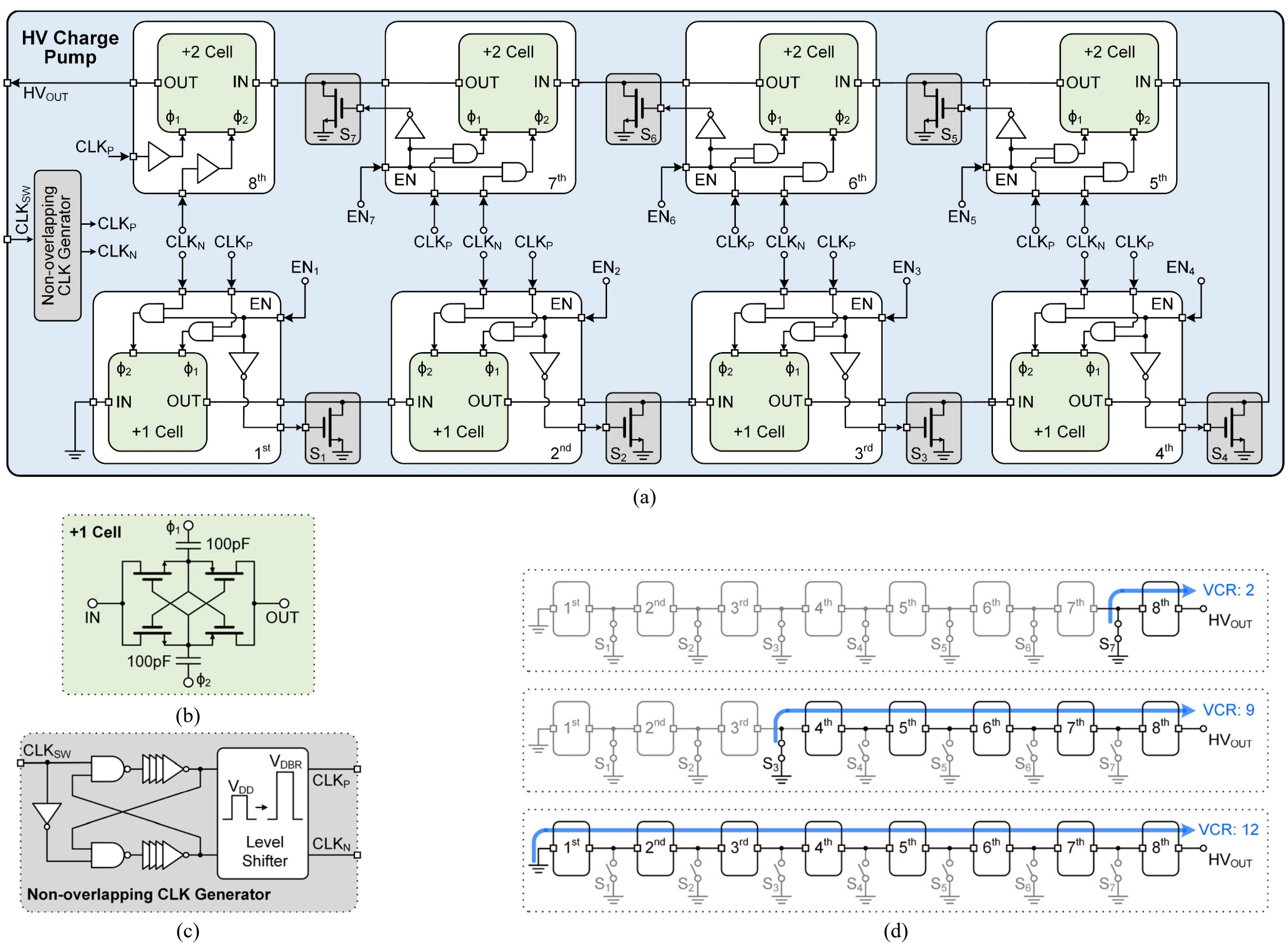

Fig. 3. Schematic diagram of (a) the HVCP, (b) the cross-coupled charge pump +1 cell, and (c) the non-overlapping CLK generator, along with (d) three examples of VCR tunning via control signals $EN_{<1-7>}$.

This article has been accepted for publication in IEEE Transactions on Biomedical Circuits and Systems. This is the author's version which has not been fully edited and content may change prior to final publication. Citation information: DOI 10.1109/TBCAS.2022.3178581

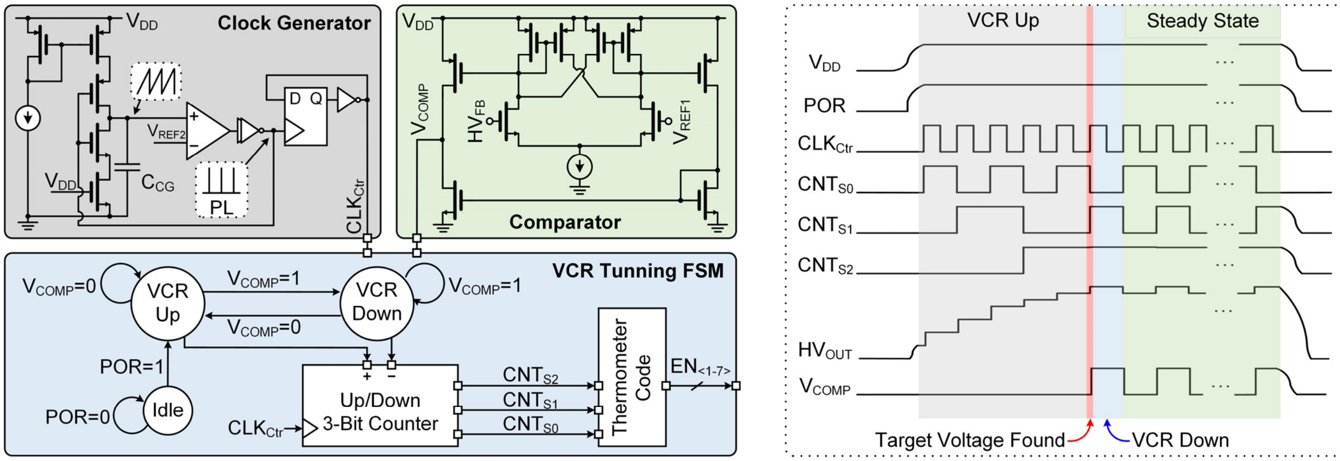

(a) (b)

Fig. 4. (a) Schematic diagrams of the clock generator, the comparator, and the VCR tunning FSM in the VCR tuning control. (b) Timing diagram of the VCR tuning control operation.

their corresponding HV switches off while keeping the remaining switches on. The VCR is set to the maximum when all the cells are enabled by turning S_1-S_7 off. Given that the 5th – 8th cells are +2 cells, if the 4th – 8th cells are enabled by turning S_4 – S_7 off while turning S_1 – S_3 on, VCR is set to 9. If all the switches are on, only the 8th cell is enabled, resulting in VCR being equal to 2.

Fig. 4 shows the schematic and timing diagrams of the VCR tunning control. As shown in Fig. 4a, the VCR tunning control circuits include two clock generators, a comparator, and a VCR tunning finite-state-machine (FSM). The clock generators use the same circuit topology, i.e., comparator-based relaxation oscillator [38]. They provide a 110 kHz clock, CLK_{SW}, for the HVCP capacitor switching and a 15 kHz clock, CLK_{Ctr}, for the control of VCR tunning FSM, respectively. In the clock generator, the comparator output, *PL*, controls the charging and discharging of the capacitor, C_{CG}. When *PL* is low, a constant current from the current source continuously charges C_{CG} while the voltage across C_{CG} increases accordingly. When the voltage across C_{CG} reaches V_{REF2}, *PL* goes high. This allows a large current to discharge C_{CG}, resulting in narrow *PL* pulses. Then, the frequency divider converts *PL* pulses to a square wave output. This clock generator is a simple and low-power design.

The VCR tunning FSM has three statuses: *Idle*, *VCR Up*, and *VCR Down*. The comparator compares HV_{FB} and V_{REF1}. According to the comparison result, V_{COMP}, the VCR tuning FSM switches between the three statues at the frequency of CLK_{Ctr}. The 3-bit counter counts down in the *VCR Down* status while counting up in the *VCR Up* status. The thermometer code circuit converts the counter outputs, CNT_{S0}-CNT_{S2}, to the 7-bit control signals, $EN_{<1\text{-}7>}$. The VCR tunning FSM sends $EN_{<1\text{-}7>}$ to the HVCP to selectively enable or disable the HVCP cells, thus adjusting the VCR and stabilizing HV_{OUT} to a target voltage in a closed-loop.

In Fig. 4b, the timing diagram shows that as the POR flag raises, the VCR tunning starts operation (i.e., the VCR tunning FSM exits the *Idle* status). HV_{FB} is detected and compared with V_{REF1} continuously. In the beginning, since HV_{OUT} is much smaller than its target voltage, HV_{FB} is lower than V_{REF1}, resulting in V_{COMP} = 0. Then, the VCR tunning FSM enters the *VCR Up*. In the *VCR Up* status, CNT_{S0}-CNT_{S2}, in which CNT_{S2} is the most significant bit (MSB), is counting up, while the number of HVCP cells being enabled is increasing, thus HV_{OUT} increases step by step towards the target voltage. When HV_{OUT} reaches the target voltage, HV_{FB} becomes larger than V_{REF1} while the comparator flips its output. Since V_{COMP} = 1 now, the VCR tunning FSM switches to the *VCR Down* status, in which the counter switches to stepping down mode. Hence, as the number of HVCP cells being enabled reduces, *VCR* and HV_{OUT} decrease. When HV_{OUT} becomes smaller than the target voltage, the VCR tuning FSM switches back to the *VCR Up* status. In steady status, the FSM switches between *VCR Up* and *VCR Down*. In the meanwhile, as CNT_{S0}-CNT_{S2} switches between two adjacent values (e.g., “110” and “101” in Fig. 4b), VCR switches between two adjacent ratios, and HV_{OUT} is bouncing around the target voltage.

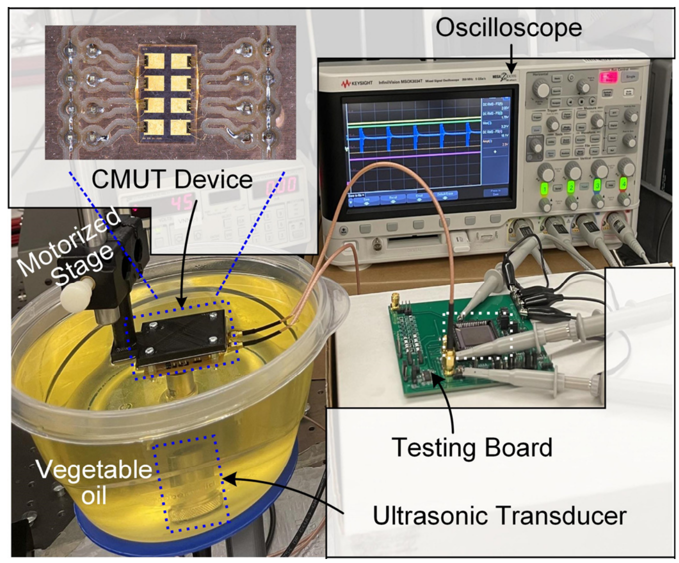

Fig. 5. Acoustic experimental setup: CMUT harvesting ultrasound power to operate the IC while the VCR tunning control stabilizes the CMUT bias voltage at a target voltage.

This article has been accepted for publication in IEEE Transactions on Biomedical Circuits and Systems. This is the author's version which has not been fully edited and content may change prior to final publication. Citation information: DOI 10.1109/TBCAS.2022.3178581

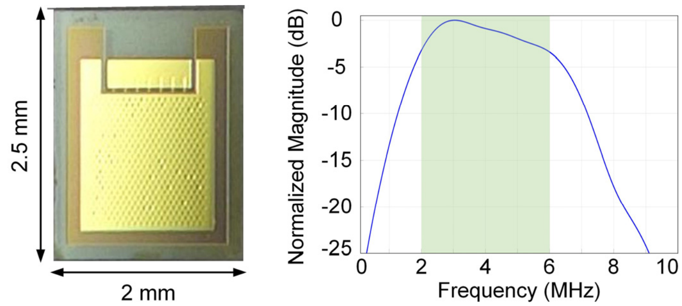

(a) (b)

Fig. 6. The implementation of the pre-charged CMUT device (b) measured CMUT frequency response.

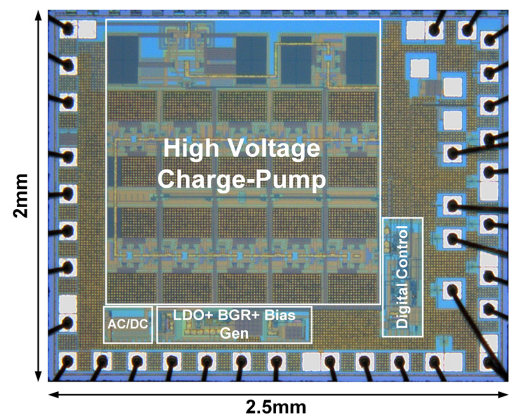

Fig. 7. The micrograph of the fabricated ultrasonic energy harvesting IC.

III. Acoustic Measurement

Fig. 5 shows the acoustic measurement setup for extensive characterizations of the proposed IC with ultrasonic powering at a focal depth of 19 mm. Multiple pre-charged CMUT devices are bonded on a printed circuit board (PCB), but only one of them connects to the IC and receives ultrasonic power. The PCB is held by a motorized stage and immersed in vegetable oil. Eventually, the CMUT will be implanted in the subject's body while performing ultrasonic energy harvesting. Vegetable oil is an insulator and also can model the acoustic impedance and loss of soft tissue.

In Fig. 6a, the fabricated single element CMUT includes 318 cells with a diameter of 60 µm, resulting in an area of 2 × 2.5 mm^2, which is designed to be assembled on the chip to be built as a miniature implantable device. In Fig. 6b, the measured frequency response shows that the pre-charged CMUT has a bandwidth of 2 MHz – 6 MHz with a peak at ~ 3 MHz. The details on the design and fabrication of the pre-charged CMUT with a metal floating gate can be found in [36].

A focused single-element commercial ultrasound Tx transducer (OLYMPUS, V325) with a focal distance of 19 mm is mounted at the bottom of the oil tank and delivers ultrasonic power pulses to the CMUT device. Alignment is applied to the motorized stage to locate the CMUT device at the focal point of the Tx transducer. The Tx transducer establishes an ultrasonic link through the oil with the CMUT. We used a hydrophone (ONDA, HGL) for the acoustic intensity measurement. The testing board carries the IC in a CLCC68 package and other supporting components (e.g., capacitors). The IC testing board is connected to the CMUT through coaxial cables. The die photo of the ultrasonic energy harvesting IC, shown in Fig. 7, is fabricated in the 180 nm HV BCD process and occupies a 2 × 2.5 mm^2 silicon area including testing pads.

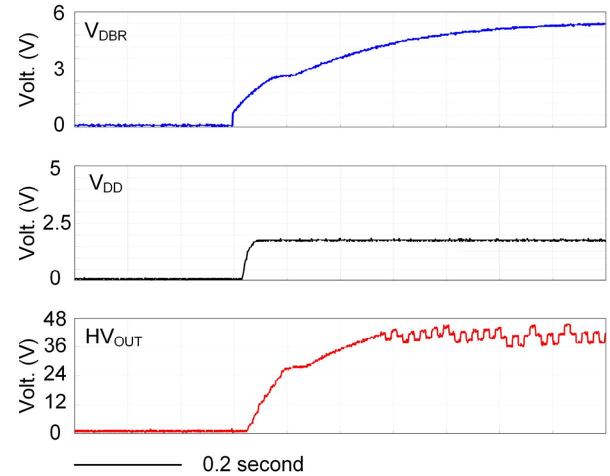

Fig. 8. Transient waveforms of the ultrasonic energy harvesting IC from starting up to going into steady status.

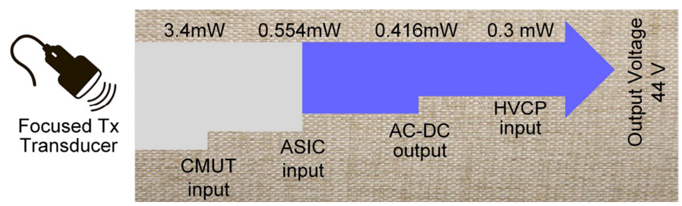

Fig. 9. Power flow from the CMUT to the HVCP in the case the HVCP offering 44V bias voltage for the CMUT.

The focused ultrasound Tx transducer delivers ultrasonic power pulses with 300 µs pulse duration at a 1 kHz pulse repetition rate to the CMUT. The acoustic intensity at the CMUT is approximately 3.78 mW/mm^2, which is below the FDA limit of 7.2 mW/mm^2. In Fig. 8, the measured starting-up transients show the process of HV_{OUT} reaching the target voltage. We set the target voltage at 44 V by tuning the resistor in the voltage divider of HV_{OUT}. Once the CMUT receives ultrasonic power and converts it to usable electrical AC input to power the IC, V_{DBR} starts increasing. After ~0.05 seconds, V_{DBR} increases to 2.2 V, and the LDO stabilizes V_{DD} to 1.8 V. In the meanwhile, the VCR tunning starts operating. The VCR tunning FSM controls VCR step up, increasing HV_{OUT}. After 0.28 seconds, as V_{DBR} increases to 4 V, HV_{OUT} reaches the target voltage of 44 V and goes into steady status, dynamically bouncing within 44 V ± 3.5 V. During the steady status. It is worthy to mention that even though V_{DBR} is still increasing, HV_{OUT} can remain in steady status thanks to the closed-loop control of HV_{OUT}.

Fig. 9 shows the power necessary at each stage from the CMUT to the HVCP when the HVCP generates a 44 V bias voltage. Given that the acoustic intensity is 3.78 mW/mm^2 at the CMUT surface and the CMUT active area for receiving energy is ~0.9 mm^2, the amount of ultrasonic power received by the CMUT is 3.4 mW. Furthermore, the CMUT converts the

This article has been accepted for publication in IEEE Transactions on Biomedical Circuits and Systems. This is the author's version which has not been fully edited and content may change prior to final publication. Citation information: DOI 10.1109/TBCAS.2022.3178581

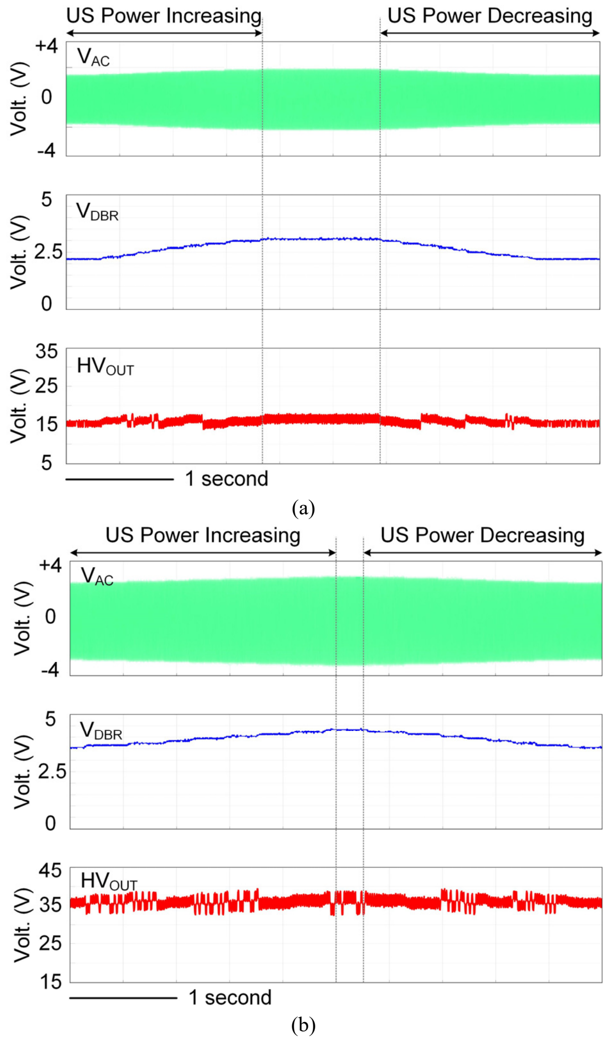

Fig. 10. Transient waveforms of closed-loop control HV_{OUT} to the target voltage of (a) 16 V and (b) 36 V when the input ultrasonic power is varying.

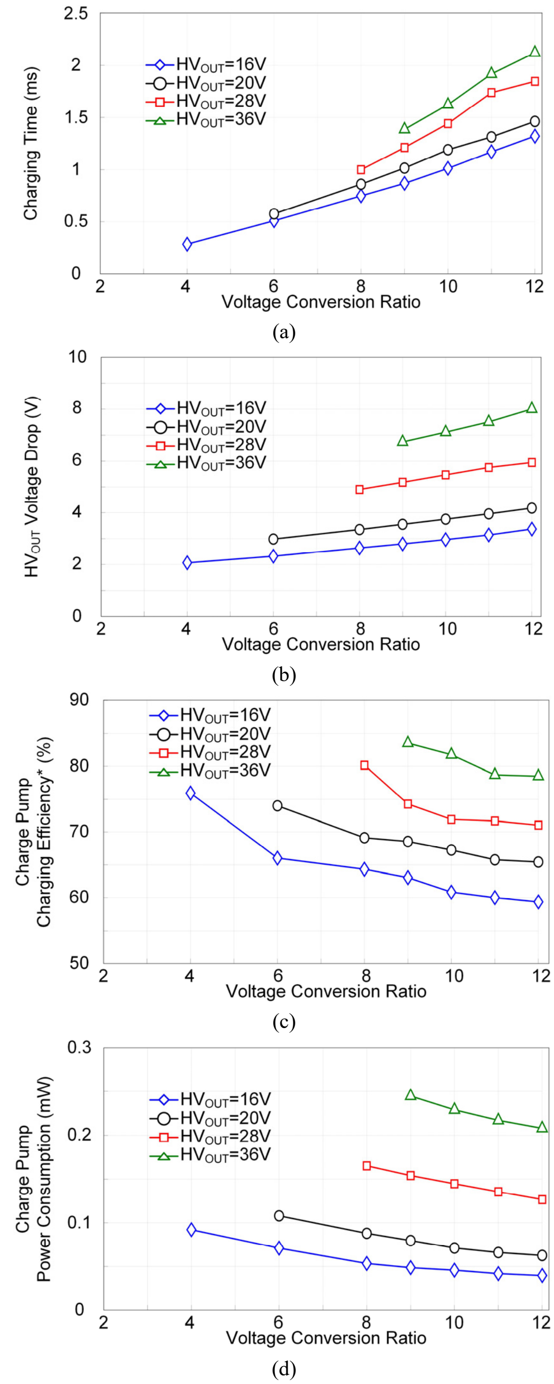

Fig. 11. Measured specifications of HVCP in terms of (a) charging time, (b) voltage drop, (c) charging efficiency, and (d) power consumption.

ultrasonic power to usable electrical power and delivers 0.554 mW to the IC. With a PTE of 75%, the DC power at the output of the voltage doubler is 0.416 mW, 72% of which is used for HVCP to generate the 44 V bias voltage.

IV. Circuit Characterization

We set the HV_{OUT} target voltage to 16 V and 36 V, respectively. Fig. 10 shows the transient waveforms of VCR tunning control when the transmitted ultrasonic power is manually increased and then decreased. In steady status, HV_{OUT} maintains bouncing within 16 V ± 1.2 V and 36 V ± 2.5 V windows, respectively, in the presence of transmitted ultrasonic power varying. In Fig. 10a, the amplitude of the received AC input voltage, V_{AC}, gradually increases following the transmitted ultrasonic power increase within the first ~2 seconds. Hence, the voltage doubler output, V_{DBR}, gradually increases. Since $HV_{OUT} = V_{DBR} \times \text{VCR} - \text{voltage loss}$, HV_{OUT} shows slight increases, which triggers the closed-loop control. Then, the VCR tunning FSM reduces VCR to compensate for the V_{DBR} increase. At ~3 seconds, the transmitted ultrasonic power starts decreasing to its original value, V_{AC} and V_{DBR} also reduce, while the VCR tunning FSM increases VCR to opposite the V_{DBR} reduction. During this process, the VCR tunning control stabilizes HV_{OUT} to the target voltage of 16 V with an offset of ± 1.2 V. In Fig. 10b, the target voltage is set to 36 V. Higher V_{AC} and V_{DBR} are required for HV_{OUT} to reach the target voltage. In the steady status, since VCR switches between two adjacent ratios, HV_{OUT} bounds around 36 V with an offset of ± 2.5 V. The HV_{OUT} offset is determined by V_{DBR}. Hence, the higher V_{DBR} is, the larger the offset is. Several reasons would influence the amount of received power, such as misalignments, the amount of

TABLE I: MEASURED SPECIFICATIONS OF THE ULTRASONIC ENERGY HARVESTING IC

IC Overview	
Chip area	2×2.5 mm^2
Average power consumption	35 μW @ HV_{OUT} = 4 V 554 μW@ HV_{OUT} = 44 V
Charge-Pump Circuit	
HV_{OUT} range	4 V – 44 V
Charging efficiency*	55% – 89%
Charging time*	0.07 ms – 2.6 ms
Voltage drop*	0.4 V – 9 V
Power consumption*	6 μW – 300 μW
HV_{OUT} offset*	0.8 V – 3 V
AC-DC Voltage Doubler	
Efficiency vs. frequency	60% – 79%
Efficiency vs. V_{AC} amplitude	70% – 76%
Efficiency vs. load power	73% – 79%
CMUT Device	
CMUT device size	2×2.5 mm^2
Collapse voltage	60 V – 65 V
Bandwidth	2 MHz – 6 MHz

*The HVCP performance when HV_{OUT} changes from 4 V to 44 V.

transmitted power variation, and load variation. The importance is to verify the robustness of the ultrasonic powering in the presence of the received power varying. The results in Fig. 10 show the compensation ability of the closed-loop VCR tunning control to the disturbs in the received power amount.

Fig. 11 shows the measured HVCP specifications at different target voltages, which are practical bias voltages for pre-charged CMUT in most cases. The HVCP drives a capacitive load of 100 pF, i.e., the equivalent capacitance of CMUT. Each curve represents an HVCP specification measured at different VCRs for the same HV_{OUT} target voltage. To meet a certain target voltage, HV_{OUT} requires a lower V_{DBR} as the VCR increases. Besides, for the same VCR, a higher HV_{OUT} target voltage requires a larger V_{DBR}.

As shown in Fig. 11a, HV_{OUT} needs a longer time to reach a higher target voltage for the same VCR. This is because the required V_{DBR} is larger and toggling the capacitors between V_{DBR} and GND in each HVSP cell takes a longer time. On the other hand, as the VCR increases, the HVCP spends a longer time charging the CMUT to reach the target voltage because the impedance looking into the output of the HVCP increases. Charging time within 0.285 ms – 2.1 ms is measured.

The voltage loss from each stage adds up at the HVCP output. In Fig. 11b, for the same HV_{OUT} target voltage when the VCR increases, the HV_{OUT} drop increases. At the same VCR, the HV_{OUT} drop increases as the HV_{OUT} target voltage increases. The step size HV_{OUT} increasing is decided by V_{DBR}. A larger HV_{OUT} requires a larger V_{DBR}. As the step size increases, the HV_{OUT} drop from each stage increases. We measured that the HV_{OUT} drop is within the range of 2 V – 8 V.

In Fig. 11c, the measured charging efficiency is 59%–83%. The charging efficiency is calculated as the stored DC energy in the 100 pF equivalent capacitance of CMUT over the total input energy of the HVCP during the charging period. For each curve, larger VCR results in lower charging efficiency for two reasons. First, the HV_{OUT} drop adds up from each stage and increases. Second, the impedance looking into the HVCP output increases as the VCR increase. On the other hand, the charging efficiency

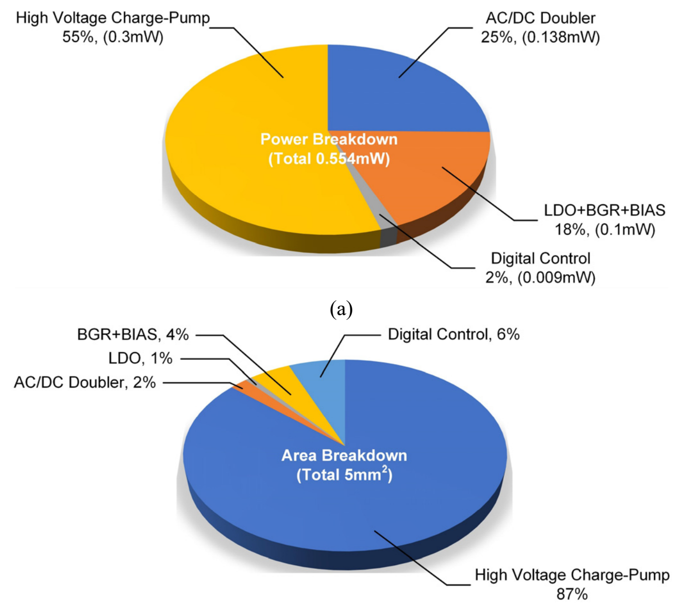

Fig. 12. (a) Average power consumption and (b) silicon area of the main circuits when HV_{OUT} = 44 V with VCR = 12.

increases as HV_{OUT} increases at the same VCR because the amount of the output energy increase is larger than that of the energy consumption.

Thanks to the simplified switch driver design, the HVCP including digital control and drivers has a low power consumption of 0.04 mW – 0.24 mW when HV_{OUT} = 16 V – 36 V. For each curve, the lower HVCP power consumption is observed as the VCR increases. V_{DBR} is the supply of the drivers in HVCP. As the required V_{DBR} is reduced, the power consumption of the drivers reduces. In contrast, for the same VCR, the required V_{DBR} is higher, resulting in higher power consumption of drivers and HVCP.

The pie charts in Fig. 12 show the average power consumption and silicon area of the main circuit blocks when the HVCP generates the highest output of 44 V with VCR = 12. As shown in Fig. 12a, the total average power consumption is 0.554 mW. More specifically, the HVCP has the highest power consumption (55%) followed by the voltage doubler (25%), other power management circuits (18%), and digital control circuit (2%). According to Fig. 12b, 87% of the total active silicon area is occupied by the HVCP. Table I summarizes the measured specifications of the IC.

V. DISCUSSION

Table II summarizes the performance of ultrasonic energy harvesting using pre-charged CMUT and compares it with state-of-the-art energy harvesting modalities used for IMDs. EM energy can propagate relatively long distances through the air. As shown in [20], the Tx antenna can deliver sufficient power at 10 cm away from the implant. However, the distance the EM propagates in tissue at high frequency (e.g., GHz bands) is much reduced. For example, the near-field inductive link approaches in [15-17] have limited power transmission distance, i.e., a few millimeters. For the applications that are not constrained to the transcutaneous power transmission, EM WPT would be a simple setup as the EM WPT approach can typically tolerate an air gap between the Tx and the body. In contrast, the ultrasonic WPT requires acoustic contact at the Tx-body interface.

In EM wireless powering, as the Rx coil becomes smaller, the power carrier frequency needs to be increased to improve the Q-factor of the tiny coil. However, the tissue absorption rate increases along with the carrier frequency. In comparison to the EM WPT approach, ultrasound energy, which is typically at lower carrier frequencies, e.g., at a few MHz orders, has lowered attenuation in tissue. Hence, ultrasonic WPT can potentially substitute or complement the EM WPT approach when powering tiny implants in deep tissue (e.g., tens of millimeters).

The piezoelectric transducer is a common power Rx component in ultrasonic WPT setup [24-26]. The implant in [24] received sufficient ultrasonic power at the tissue depth of 10.5 cm. In [25] and [26], the ultrasonic-powered implants can operate safely in vivo at the tissue depth of 18 mm and 50 mm, respectively. The implants presented in [24-26] have a common feature that both the piezo and IC are bonded onto a substrate. Recently, CMUT has been shown to be a viable alternative to piezoelectric transducers because of its easy integration with circuits, CMUT-on-CMOS. The monolithic CMUT-on-CMOS approach also enables minimized parasitic. Driven by the need of shrinking the size of the implants, CMUTs can be used as the power Rx component in implants. However, CMUTs need a high bias voltage, such as several tens of volts to hundred volts. The recent emerging pre-charged CMUTs, which can relax the need for a high bias voltage significantly, enhance the wide use of CMUT power Rx in implants. Our proposed approach of pre-charged CMUT energy harvesting compares favorably with the existing piezo-based ultrasonic WPT approaches in terms of the moderate power transmission depth, the acoustic intensity, and the amount of power delivery to the IC.

We used a single-element commercial Tx transducer with a focal depth of 19 mm only for testing purposes. In the experimental characterization the goal is to have a spot size commensurate with the physical size of the receiving CMUT, a transmission frequency close to the center peak of the CMUT, and an acoustic intensity above the minimum acoustic intensity needed to operate the IC but below the FDA limit of 7.2 mW/mm^2. This is to characterize the performance of the power receiving unit. In a setting where the implant is deeper, we can use a larger aperture Tx transducer focusing on the Rx to ensure the same acoustic intensity and spot size.

The ultrasonic power at the transducer surface is approximately 27.8 mW. As shown in Fig. 9, the amount of ultrasonic power received by the CMUT at 19 mm depth is 3.4 mW, and the usable electrical power delivered to the IC is 0.554 mW, yielding a PTE from ultrasonic power at the Tx transducer to electrical power at the IC of 2%. The total PTE is mainly influenced by the attenuation in media (such as tissue, oil, etc.), the electrical-to-acoustic power conversion efficiency of the Tx transducer, and the acoustic-to-electrical power conversion efficiency of the power Rx component (i.e., CMUT or piezo). The wireless powering PTE is limited by our current experimental setup due to the use of the commercial ultrasound Tx transducer. The ultrasonic powering PTE can be further improved by designing a custom Tx array and/or optimizing its conversion efficiency [27, 28].

In our current experimental setup, we need to first test the amount of trapped charge to decide the optimal DC bias needed for the pre-charged CMUT to maximize its output power. Then, we can set the target value of HV_{OUT} to the optimal DC bias value by tuning the resistor in the voltage divider manually. In our future work, we will add on-chip auto-tuning of the resistor so that the IC will search for the optimal target voltage of HV_{OUT} automatically. A viable operation process could be that in the default setting, the auto-tuning mechanism will set the target voltage of HV_{OUT} to a value and increase the target voltage again once HV_{OUT} reaches the voltage. Upon HV_{OUT} reaches the collapse voltage of the pre-charged CMUT, the auto-tuning mechanism will reduce the target voltage of HV_{OUT} by one step and stabilize it at its current status.

When WPT condition changes, e.g., misalignments, amount of transmitted power varying, and load varying, if the CMUT still can harvest sufficient power such that the HVCP can provide the optimal bias voltage, the closed-loop tuning control will dynamically adjust VCR to compensate for the wireless powering variations, stabilizing HV_{OUT} at the optimal value. In cases that the CMUT cannot receive sufficient ultrasonic power, we need to adjust the amount of the transmitted power to compensate for the WPT variations. To do so, we will enable wireless data communication in our future work such that the IC will send the information of the received power to the Tx

TABLE II: COMPARISON WITH STATE-OF-THE-ART ENERGY HARVESTING MODALITIES USED FOR IMDS

Publications	[15]	[16]	[17]	[20]	[24]	[25]	**This Work**
Technology	350 nm CMOS	65 nm CMOS	130 nm CMOS	COTS	180 nm HV BCD	65 nm CMOS	**180 nm HV BCD**
Wireless power modality	3-coil inductive link	2-coil inductive link	2-coil inductive link	RF link	Ultrasonic link	Ultrasonic link	**Ultrasonic link**
Carrier frequency	60 MHz	1 GHz	1.3 GHz	1.8 GHz, 2.9 GHz	1.314 MHz	1.85 MHz	**2 – 6 MHz**
Power receiver	Wire-wound coil, 1.6 mm diameter	On-chip coil, 500 µm diameter	On-chip coil, 200 µm diameter	Antenna	Piezoelectric transducer	Piezoelectric transducer	**Pre-charged CMUT**
Acoustic intensity	N/A	N/A	N/A	N/A	2.9 mW/mm^2	> 56 mW/cm^2	**3.78 mW/mm^2**
Medium	Tissue	Tissue	Tissue	Air + Tissue	Oil	Gel / Tissue	**Oil**
Transmission range	7 mm	8 mm	5 mm	10 cm through air	10.5 cm	70 mm (gel), 55 mm tissue	**19 mm**
High DC voltage generator	Voltage doubler	Rectifier	Charge pump rectifier	Rectifier	Charge pump	Rectifier	**HVCP**
High voltage output	5 V	N/A	>1.2 V	N/A	15 V	3 V	**4 V – 44 V**

through the ultrasonic link while the Tx transducer adjusts the amount of transmitted power correspondingly.

The focus of this paper is on the design and measurement of the IC that interfaces with a pre-charged CMUT for ultrasonic energy harvesting. We characterized the IC specifications and demonstrated the proof-of-concept ultrasonic energy harvesting using the pre-charged CMUT. Implementation of a miniature (mm-sized) device with the CMUT and IC stacked together as shown in Fig. 1 is part of our future work. The HVCP design can also be readily extended to neural stimulation applications, where the stimulators need to have high compliance voltage to tolerate the voltage across the tissue-electrode interface impedance [39, 40]. With such feasibilities, the extension of the current IC to a wireless implantable stimulator is readily possible. Moreover, stimulators with modified form factors can be suited for certain stimulation targets, such as assembled with cuff electrodes for peripheral nerve stimulation [25].

VI. Conclusion

We have presented an ultrasonic energy harvesting IC in which a novel low power, OVS robust, adaptive HVCP is implemented. To the best of our knowledge, this is the first IC that interfaces with pre-charged CMUT for ultrasonic energy harvesting. The circuit topology of the HVCP is chosen for not only power efficiency but also design simplicity and reliability. The proposed HVCP can generate an adjustable output voltage within the range of 4 V – 44 V, which can tolerate a wide variety of needs for bias voltage under different pre-charged CMUT conditions. Besides, the output voltage can be stabilized to a target voltage by the closed-loop VCR tuning mechanism in the presence of wireless power conditions varying.

Acknowledgments

Ömer Oralkan is an inventor on patents related to CMUT fabrication on glass substrates and a co-founder of ClearSens, Inc., Morrisville, NC, USA, which has licensed some of these patents.

References

[1] R. Das, F. Moradi and H. Heidari, "Biointegrated and wirelessly powered implantable brain devices: a review," *IEEE Trans. Biomed. Circuits Syst.*, vol. 14, no. 2, pp. 343-358, Apr. 2020.

[2] A. Vázquez-Guardado, Y. Yang, A. J. Bandodkar, and J. A. Rogers. "Recent advances in neurotechnologies with broad potential for neuroscience research," *Nat. Neurosci.*, vol. 23, no. 12, pp. 1522-1536, Nov. 2020.

[3] L. Luan, J. T. Robinson, B. Aazhang, T. Chi, K. Yang, X. Li, H. Rathore et al. "Recent advances in electrical neural interface engineering: minimal invasiveness, longevity, and scalability." *Neuron* 108, no. 2, pp. 302-321, Oct. 2020.

[4] A. Ibrahim, M. Meng and M. Kiani, "A comprehensive comparative study on inductive and ultrasonic wireless power transmission to biomedical implants," *IEEE Sens. J.*, vol. 18, no. 9, pp. 3813-3826, May 2018.

[5] S. R. Khan, S. K. Pavuluri, G. Cummins, and M. P. Desmulliez, " Wireless power transfer techniques for implantable medical devices: a review," *Sensors*, vol. 20, no. 12, p. 3487, June 2020.

[6] B. Lee and Y. Jia, "Wirelessly-powered cage designs for supporting long-term experiments on small freely behaving animals in a large experimental arena," Electronics, vol. 9, no. 12, p. 1999, Nov. 2020.

[7] Y. Jia, S. A. Mirbozorgi, Z. Wang, C. Hsu, T. E. Madsen, D. Rainnie, and M. Ghovanloo, "Position and orientation insensitive wireless power transmission for EnerCage-Homecage system," *IEEE Trans. Biomed. Eng.*, vol. 64, no. 10, pp. 2439-2449, Oct. 2017.

[8] S. A. Mirbozorgi, Y. Jia, D. Canales, and M. Ghovanloo, "A wirelessly-powered homecage with segmented copper foils and closed-loop power control," *IEEE Trans. Biomed. Circuits Syst.*, vol. 10, no. 5, pp. 979-989, Oct. 2016.

[9] K. -W. Yang, K. Oh and S. Ha, "Challenges in scaling down of free-floating implantable neural interfaces to millimeter scale," *IEEE Access*, vol. 8, pp. 133295-133320, July 2020.

[10] G. L. Barbruni, P. M. Ros, D. Demarchi, S. Carrara and D. Ghezzi, "Miniaturised wireless power transfer systems for neurostimulation: a review," *IEEE Trans. Biomed. Circuits Syst*., vol. 14, no. 6, pp. 1160-1178, Dec. 2020.

[11] N. Soltani, M. ElAnsary, J. Xu, J. S. Filho, and R. Genov, "Safety-optimized inductive powering of implantable medical devices: tutorial and comprehensive design guide," *IEEE Trans. Biomed. Circuits Syst.*, vol. 15, no. 6, pp. 1354-1367, Dec. 2021.

[12] A. Ibrahim and M. Kiani, "A figure-of-merit for design and optimization of inductive power transmission links for millimeter-sized biomedical implants," *IEEE Trans. Biomed. Circuits Syst*., vol. 10, no. 6, pp. 1100-1111, Dec. 2016.

[13] S. A. Mirbozorgi, P. Yeon, and M. Ghovanloo, "Robust wireless power transmission to mm-sized free-floating distributed implants," *IEEE Trans. Biomed. Circuits Syst.*, vol. 11, no. 3, pp. 692–702, June 2017.

[14] P. Yeon, S. A. Mirbozorgi, J. Lim, and M. Ghovanloo, "Feasibility study on active back telemetry and power transmission through an inductive link for millimeter-sized biomedical implants," *IEEE Trans. Biomed. Circuits Syst.*, vol. 11, no. 6, pp. 1366–1376, Dec. 2017.

[15] Y. Jia, S. A. Mirbozorgi, B. Lee, W. Khan, F. Madi, O. T. Inan, A. Weber, W. Li, and M. Ghovanloo, "A mm-sized free-floating wirelessly powered implantable optical stimulation device," *IEEE Trans. Biomed. Circuits Syst.*, vol. 13, no. 4, pp. 608-618, Aug. 2019.

[16] J. Lee, V. Leung, A. H. Lee, J. Huang, P. Asbeck, P. P. Mercier, S. Shellhammer, L. Larson, F. Laiwalla, and A. Nurmikko. "Neural recording and stimulation using wireless networks of microimplants," *Nat. Electron.*, vol. 4, no. 8, pp. 604-614, Aug. 2021.

[17] A. Khalifa, Y. Karimi, Q. Wang, S. Garikapati, W. Montlouis, M. Stanaćević, N. Thakor, and R. Etienne-Cummings, "The microbead: a highly miniaturized wirelessly powered implantable neural stimulating system," *IEEE Trans. Biomed. Circuits Syst.*, vol. 12, no. 3, pp. 521-531, June 2018.

[18] IEEE Standard for Safety Levels with Respect to Human Exposure to Radio Frequency Electromagnetic Fields, 3 kHz to 300 GHz, IEEE Standard C95.1-2005. 2005.

[19] Y. Tanabe, J. S. Ho, J. Liu, S. Y. Liao, Z. Zhen, S. Hsu, C. Shuto, Z. Y. Zhu, A. Ma, C. Vassos. P. Chen, H. G. Tse, A. S. Poon, "High-performance wireless powering for peripheral nerve neuromodulation systems," PLoS One, vol. 12, no. 10, e0186698, Oct. 2017.

[20] K. N. Noh, S. Park. R. Qazi, Z. Zou, A.D. Mickle, J.G. Grajales-Reyes, K. Jang, R.W. Gereau, J. Xiao, J.A. Rogers, and J. Jeong, "Miniaturized, battery-free optofluidic systems with potential for wireless pharmacology and optogenetics," *Small*, vol. 14, no. 4, p. 1702479, Jan. 2018.

[21] R. V. Taalla, M. S. Arefin, A. Kaynak and A. Z. Kouzani, "A review on miniaturized ultrasonic wireless power transfer to implantable medical devices," *IEEE Access*, vol. 7, pp. 2092-2106, Jan. 2019.

[22] M. Meng and M. Kiani, "Design and optimization of ultrasonic wireless power transmission links for millimeter-sized biomedical implants," *IEEE Trans. Biomed. Circuits Syst.*, vol. 11, no. 1, pp. 98-107, Feb. 2017.

[23] Food and Drug Administration (FDA), "Information for manufacturers seeking marketing clearance of diagnostic ultrasound systems and transducers" *Guidance for Industry and FDA Staff*, Sept. 2008.

[24] J. Charthad, T. Chang, Z. Liu, A. Sawaby, M. J. Weber, S. Baker, F. Gore, S. A. Felt, and A. Arbabian, "A mm-sized wireless implantable device for electrical stimulation of peripheral nerves," *IEEE Trans. Biomed. Circuits Syst.*, vol. 12, no. 2, pp. 257-270, Apr. 2018.

[25] D. K. Piech, B. C. Johnson, K. Shen, M. M. Ghanbari, K. Y. Li, R. M. Neely, J. E. Kay, J. M. Carmena, M. M. Maharbiz, and R. Muller. "A wireless millimetre-scale implantable neural stimulator with

ultrasonically powered bidirectional communication," *Nat. Biomed. Eng.*, vol. 4, no. 2, pp. 207-222, Feb. 2020.

[26] S. Sonmezoglu and M. M. Maharbiz, "A 4.5mm^3 deep-tissue ultrasonic implantable luminescence oxygen sensor," *2020 IEEE International Solid-State Circuits Conference (ISSCC)*, 2020, pp. 454-456.

[27] Z. Kashani, S. J. J. Ilham, and M. Kiani, "Design and optimization of ultrasonic links with phased arrays for wireless power transmission to biomedical implants," *IEEE Trans. Biomed. Circuits Syst.* (Early Access), Jan. 2022.

[28] B. C. Benedict, M. M. Ghanbari, and R. Muller. "Phased array beamforming methods for powering biomedical ultrasonic implants," arXiv preprint arXiv:2203.01493, Mar. 2022.

[29] J. Joseph, B. Ma, and B. T. Khuri-Yakub, "Applications of capacitive micromachined ultrasonic transducers: a comprehensive review," *IEEE Trans. Ultrason. Ferroelectr. Freq. Control*, vol. 69, no. 2, pp. 456-467, Feb. 2022.

[30] K. Brenner, A. S. Ergun, K. Firouzi, M. F. Rasmussen, Q. Stedman, and B. Khuri–Yakub, "Advances in capacitive micromachined ultrasonic transducers," *Micromachines*, vol. 10, no. 2, p. 152. Feb. 2019.

[31] J. Jung, W. Lee, W. Kang, E. Shin, J. Ryu, and H. Choi, "Review of piezoelectric micromachined ultrasonic transducers and their applications," *J. Micromech. Microeng.*, vol. 27, no. 11, p. 113001, Sept. 2017.

[32] F. L. Degertekin, "Microscale systems based on ultrasonic MEMS — CMOS integration," 2017 19th International Conference on Solid-State Sensors, Actuators and Microsystems (TRANSDUCERS), 2017, pp. 397-401.

[33] C. Seok, O. J. Adelegan, A. Ö. Biliroğlu, F. Y. Yamaner and Ö. Oralkan, "A wearable ultrasonic neurostimulator—Part II: a 2D CMUT phased array system with a flip-chip bonded ASIC," *IEEE Trans. Biomed. Circuits Syst.*, vol. 15, no. 4, pp. 705-718, Aug. 2021.

[34] K. K. Park, M. Kupnik, H. J. Lee, Ö. Oralkan and B. T. Khuri-Yakub, "Zero-bias resonant sensor with an oxide-nitride layer as charge trap," SENSORS, 2010 IEEE, 2010, pp. 1024-1028.

[35] M. Ho, M. Kupnik, K. K. Park and B. T. Khuri-Yakub, "Long-term measurement results of pre-charged CMUTs with zero external bias operation," 2012 IEEE International Ultrasonics Symposium, 2012, pp. 89-92.

[36] M. Annayev, O. J. Adelegan, F. Y. Yamaner and Ö. Oralkan, "Design of pre-charged CMUTs with a metal floating Gate," *2021 IEEE International Ultrasonics Symposium (IUS)*, 2021, pp. 1-3.

[37] Z. Luo, L. C. Yu, and M. D. Ker, "An efficient, wide-output, high-voltage charge pump with a stage selection circuit realized in a low-voltage CMOS process," *IEEE Trans. Circuits Syst. I: Regular Papers*, vol. 66, no. 9, pp. 3437-3444, Sept. 2019.

[38] R. J. Baker, "Special purpose CMOS circuits," in *CMOS circuit design, layout, and simulation*, 3nd ed. Hoboken, NJ, U.S.: John Wiley & Sons, Inc., 2010, pp. 523-529.

[39] H. Pu, O. Malekzadeh-Arasteh, A. R. Danesh, Z. Nenadic, A. H. Do and P. Heydari, "A CMOS dual-mode brain-computer interface chipset with 2-mV precision time-based charge balancing and stimulation-side artifact suppression," *IEEE J. Solid-State Circuits* (Early Access), 2022.

[40] T. Y. Yen and M. D. Ker, "Design of dual-mode stimulus chip with built-in high voltage generator for biomedical applications," *IEEE Trans. Biomed. Circuits Syst.*, vol. 14, no. 5, pp. 961-970, Oct. 2020.

Linran Zhao (Graduate Student Member, IEEE) received his B.S. degree from the University of Electronic Science and Technology of China, Chengdu, China, in 2017 and his M.S. degree from the University of California, Irvine, in 2019. Currently, he is pursuing his Ph.D. degree at The University of Texas at Austin. His research interest includes analog/mixed-signal integrated circuits, sensor interface, and wireless systems for low-power IoT devices, biomedical devices, and neural interface devices.

Muhammetgeldi Annayev (Graduate Student Member, IEEE) received his B.S. degree from the Magtymguly Turkmen State University, Ashgabat, Turkmenistan, in 2015, and his M.S. degree from North Carolina State University, Raleigh, NC, USA, in 2020, both in physics. He is currently pursuing his Ph.D. degree in electrical engineering at North Carolina State University, Raleigh, NC. His current research interests include design and fabrication of pre-charged CMUTs with a metal floating gate, dual-mode dual-frequency 1D CMUT arrays for acoustic angiography applications, and 2-D CMUT arrays incorporating through-glass interconnects.

Ömer Oralkan (Senior Member, IEEE) received the B.S. degree in electrical engineering from Bilkent University, Ankara, Turkey, in 1995, the M.S. degree in electrical engineering from Clemson University, Clemson, SC, USA, in 1997, and the Ph.D. degree in electrical engineering from Stanford University, Stanford, CA, USA, in 2004. From 2004 to 2007 and from 2007 to 2011, he was a Research Associate and then a Senior Research Associate with E. L. Ginzton Laboratory, Stanford University. In 2012, he joined North Carolina State University, Raleigh, NC, USA, where he is currently a Professor of electrical and computer engineering. He has authored more than 200 scientific publications. His current research interests include developing devices and systems for ultrasound imaging, photoacoustic imaging, image-guided therapy, biological and chemical sensing, ultrasound neural stimulation, and medical implantables. He serves on the Technical Program Committee of the IEEE International Ultrasonics Symposium. He was the recipient of the 2016 William F. Lane Outstanding Teacher Award at NC State, the 2013 DARPA Young Faculty Award, and the 2002 Outstanding Paper Award of the IEEE Ultrasonics, Ferro- electrics, and Frequency Control Society. He is the Editor-in-Chief of the IEEE OPEN ACCESS JOURNAL OF ULTRASONICS, FERROELECTRICS AND FREQUENCY CONTROL.

Yaoyao Jia (Member, IEEE) received her Ph.D. degree from Georgia Tech in 2019. From 2019 to 2021, she was an assistant professor in the electrical and computer engineering department at North Carolina State University. Currently, she is an assistant professor in the electrical and computer engineering department at the University of Texas at Austin and a Fellow of Silicon Labs Chair in electrical engineering. Dr. Jia has filed 11 patents, published 1 book chapter and 40+ papers in refereed journals and conferences. Her research primarily focuses on analog and mixed-signal integrated circuits, inductive, ultrasonic, and thermoelectric energy harvesting, the Internet of Medical Things (IoMT), implantable biomedical devices, miniature neural Interface implants, and wearable devices. Dr. Jia received the 2022 Micromachines Best Paper Awards, the 2019 IEEE Biomedical Circuits and Systems Conference (BioCAS) best paper award, the IEEE Solid-State Circuits Society (SSCS) predoctoral achievement award, and the 2015 IEEE BioCAS best live demo award. She is serving as the Associate Editor of IEEE Transactions on Biomedical Circuits and Systems (TBioCAS). She is also serving on the Technical Program Committee of IEEE Biomedical Circuits and Systems Conference (BioCAS) and IEEE Custom Integrated Circuits Conference (CICC).